catalysts

MDPI

Article

Scalability and Investigation of the Geometrical Features and Shapes of a Tandem Photo-Electrolysis Cell Based on Non-Critical Raw Materials

Carmelo Lo Vecchio *, Giosuè Giacoppo, Orazio Barbera, Alessandra Carbone, Vincenzo Baglio, Antonino Salvatore Aricò, Giuseppe Monforte and Stefano Trocino *

Consiglio Nazionale delle Ricerche, Istituto di Tecnologie Avanzate per l'Energia "Nicola Giordano", CNR-ITAE, Via Salita Santa Lucia Sopra Contesse 5, 98126 Messina, Italy; giosue.giacoppo@itae.cnr.it (G.G.); orazio.barbera@itae.cnr.it (O.B.); alessandra.carbone@itae.cnr.it (A.C.); vincenzo.baglio@itae.cnr.it (V.B.); antonino.arico@itae.cnr.it (A.S.A.); giuseppe.monforte@itae.cnr.it (G.M.)

* Correspondence: carmelo.lovecchio@itae.cnr.it (C.L.V.); stefano.trocino@itae.cnr.it (S.T.)

Abstract: Tandem photoelectrochemical cells (PECs) are devices useful for water splitting (WS) with the production of oxygen at the photoanode (PA) and hydrogen at the photocathode (PC) by adsorbing more than 75% of the solar irradiation; a portion of the UV/Vis direct solar irradiation is captured by the PA and a diffused or transmitted IR/Vis portion by the PC. Herein, Ti-doped hematite (PA) and CuO (PC) were employed as abundant and non-critical raw semiconductors characterised by proper band gap and band edge banding for the photoelectrochemical WS and absorption of sunlight. The investigation of inexpensive PEC was focused on the scalability of an active area from 0.25 cm^2 to 40 cm^2 with a rectangular or square shape. For the first time, this study introduces the novel concept of a glass electrode membrane assembly (GEMA), which was developed with an ionomeric glue to improve the interfacial contact between the membrane and photoelectrodes. On a large scale, the electron–hole recombination and the non-optimal photoelectrodes/electrolyte interface were optimized by inserting a glass support at the photocathode and drilled fluorine tin oxide (FTO) at the photoanode to ensure the flow of reagents and products. Rectangular 40 cm^2 PEC showed a larger maximum enthalpy efficiency of 0.6% compared to the square PEC, which had a value of 0.37% at a low bias-assisted voltage (−0.6 V). Furthermore, throughput efficiency reached a maximum value of 1.2% and 0.8%, demonstrating either an important effect of the PEC geometries or a non-significant variation of the photocurrent within the scalability.

Keywords: tandem PEC; hematite photoanode; CuO photocathode; geometries; hydrogen production; photoelectrochemical water splitting; large-scale photoelectrodes

Citation: Lo Vecchio, C.; Giacoppo, G.; Barbera, O.; Carbone, A.; Baglio, V.; Aricò, A.S.; Monforte, G.; Trocino, S. Scalability and Investigation of the Geometrical Features and Shapes of a Tandem Photo-Electrolysis Cell Based on Non-Critical Raw Materials. *Catalysts* **2024**, *14*, 98. https://doi.org/10.3390/catal14020098

Academic Editors: Bruno Fabre and Sang-Il Choi

Received: 21 December 2023
Revised: 15 January 2024
Accepted: 22 January 2024
Published: 24 January 2024

1. Introduction

The energy resources of our planet could be divided into three broad categories: (1) fossil fuels able to satisfy human needs in the short term, being a finite source, but with detrimental release of pollutant gases into the atmosphere [1–3]; (2) renewable resources that derive energy from solar, wind, hydroelectric, biomasses, and geothermal sources [4–8]; (3) nuclear energy [9]. Recent data for gross worldwide production of electric energy report values of 62% derived from fossil fuels, 28% from renewable sources, and about 12% from nuclear. Furthermore, the energy request is continuously increasing, forecasting a requirement of about 8.3×10^{12} Watt·s in 2021. In this global context, human beings and international politics must promptly adopt behaviours to avoid energy production from fossil fuels and encourage their overall substitution with renewable energy technologies and decarbonization [10–12]. Solar energy is the primary energy source on our Earth, and it is produced continuously at 3.83×10^{26} Watt·s. Photovoltaic panels and wind turbines represent mature technologies to convert solar and wind energy into electricity that can

be inserted into smart grid infrastructure for domestic/industrial purposes. However, during the night, cloudy weather, or non-windy days, these technologies cannot act as energy converters, which is the cause of their characteristic intermittency in power generation."Green" energy storage can be achieved through water splitting (WS) in electrolysers, with the formation of oxygen at the anode and hydrogen at the cathode [13–17]. This non-spontaneous reaction requires an energy input (1.23 V) provided by the existing grid or by renewable sources, such as the coupling of electrolysis to photovoltaic or wind devices [18,19]. Successively, the stored hydrogen can be employed as an energy carrier to convert its chemical energy into electricity by fuel cells [20–23] or fed into natural gas pipelines for decentralised energy production and remote use (cooking and heating). In centralised production, the highly pure hydrogen produced from electrolysis can be used in the chemical and semiconductor industry and for metallurgic purposes. However, the high capital cost, mainly due to the use of precious metal catalysts (Pt, Ir, etc.), represents a drawback of this technology that needs to be overcome in the future [24].

It is now recognised that the most cost-effective hydrogen production technology is the natural gas reforming with the release of CO_2 into the atmosphere. One critical aspect regarding the use of hydrogen from steam reforming is related to the presence of some traces of carbon monoxide molecules, which are inherent to the reforming process [25,26]. Their elimination requires extensive purification processes that are energy-intensive and imply the use, in some cases, of palladium/silver membranes to reach 5N hydrogen quality. However, the presence of CO molecules at trace levels causes the deterioration of fuel cell anodes as CO poisoning on Pt active sites. If CO attains a high surface coverage, the Pt surface is irreversibly poisoned. This is incompatible with the required low hydrogen oxidation overpotentials at Pt electrodes.

In contrast, photo-electrolysis is a process in which a photoelectrochemical cell (PEC) absorbs solar irradiation to split water into H_2 and O_2 through semiconductors with appropriate bandgaps for oxygen and hydrogen evolution [27,28]. This technology can be deployed in every country since no critical raw materials are needed and solar energy is abundant almost everywhere. The easily mass-producible and highly scalable technology of photo-electrolysis has the potential to eventually achieve cheaper hydrogen production than natural gas reforming plants, thereby positively impacting the sustainability of hydrogen production as no hydrocarbon molecules are involved in photo-electrolytic hydrogen generation. However, many recent works have investigated PECs in a liquid electrolyte, thus the separation of the produced fuel and oxidant and the scalability of these systems is difficult [29–32]. The photo-electrolysis device proposed here is designed to directly generate high-purity hydrogen output, which can be directly employed in fuel cells, allowing their effective implementation. A pure H_2 output stream (5N) is obtained using a solid polymer electrolyte layer, separating H_2 and O_2 combined with a hydrophobic backing layer at the CuO-based photocathode that allows H_2 to pass while retaining H_2O.

Tandem PECs are devices capable of capturing a portion of UV/Vis direct solar irradiation by a photoanode (PA) and a diffused IR/Vis portion by a photocathode (PC). The predicted solar to hydrogen (STH) efficiency value for the Fe_2O_3/CuO tandem couple was 11%, combining 2.2 eV and 1.0 eV band gap oxides [33]. Thus, the experimental value should increase by hindering recombination losses (appropriate use of co-catalysts) and optimizing interfacial components and bubble flow. In our previous studies on 0.25 cm^2 lab cells, a solid anionic membrane, separating n-type hematite and p-type CuO semiconductors, performed more efficiently than a proton exchange semiconductor [34]. Subsequently, an enhanced WS PEC was assessed by the effect of NiFe-oxide co-catalysts at the hematite/fluorine tin oxide (FTO) photoanode to reduce electron–hole recombination losses and improve the oxygen evolution reaction (OER) kinetically [35]. Another study demonstrated a suitable activity of P-and-Ti-doped hematite for the OER. Moreover, a step change in efficiency (from 0.2% to 1.2%) was achieved in a tandem critical raw material-free PEC using a CuO deposited over a hydrophobic gas diffusion layer (GDL) in substitution of the FTO at the photocathode [36]. Finally, photoelectrochemical WS with enhanced

efficiency was obtained by a nickel-based co-catalyst at a cupric oxide photocathode in the 0.25 cm^2 lab cell [37].

Herein, as a further step, an investigation of new configurations of a scale-up PEC was carried out to achieve an engineered device. Indeed, the 0.25 cm^2 active area PEC can be considered as a device suitable only for active-material characterisation. Using a small area device reduces, for instance, issues related to gas and water leakage, hydrogen and current collection, oxygen escaping, electron–hole recombination, and water feeding. Scaling the active area from 0.25 up to 40 cm^2, or reconfiguring active areas from square to rectangular, as carried out in this work, implies several construction issues, principally related to the increase in the probability of the electron–hole recombination, water/oxygen management issues, and uneven contact between the layers of the PEC.

This study has two goals based on the acquisition of two new elements of knowledge of solid electrolyte PECs: (1) To investigate how the active area and form factor (rectangular instead of square) influence the PEC's performances; (2) To introduce the novel concept of a glass electrode membrane assembly (GEMA) addressed to improve the interfacial contact between the membrane and photoelectrodes. In addition, as sketched in Figure 1a (vertical) and Figure 1c (horizontal), a drilled FTO was employed for proper water feeding of the PEC and oxygen evolution from the photoanode. Figure 1b shows the working mechanism of the Fe_2O_3/CuO tandem cell in which the valence band edge bending of the photoanode must have the potential to evolve oxygen and the conduction band edge bending of the photocathode must have a proper potential to guarantee hydrogen evolution from water splitting.

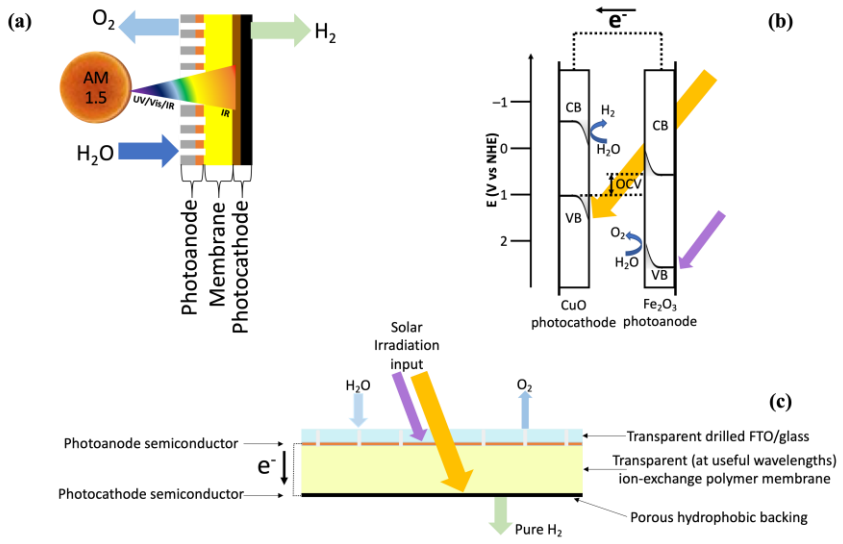

Figure 1. Sketch of a tandem PEC with drilled FTO for water feeding and oxygen escape in (**a**) vertical or (**c**) horizontal position and (**b**) working mechanism of the tandem cell.

Furthermore, the tandem 0.25 cm^2 lab cell was scaled up to 40 cm^2 and investigated in a square or rectangular configuration by evaluating the electrochemical impedance, photocurrent, efficiencies at low bias-voltage, and durability. The PECs were equipped with two earth-abundant semiconductors: Ti-doped hematite deposited over a drilled FTO at the PA and CuO sprayed over a hydrophobized GDL at the PC to allow the permeation of pure and dry hydrogen in the outlet.

This research work shows the great potential of a PEC with a solid electrolyte, to be easily scalable in view of its engineering, thus eliminating the drawbacks regarding the management of corrosive electrolytes in liquid-based cells.

2. Results

2.1. Physicochemical Characterization of Photoelectrodes

From a physicochemical point of view, X-ray diffraction (XRD), scanning electron microscopy (SEM), and transmission electron microscopy (TEM) analyses were carried out on the Ti-doped hematite photoanode as was previously reported by our group [35], confirming that the structure of hematite is characterized by nanocolumns of about 90 nm diameter length. Herein, the X-ray photoelectron spectroscopy (XPS) survey spectra of the Ti-doped hematite photoanode deposited over an FTO transparent glass are shown in Figure 2, before (Figure 2a) and after Ar sputtering for 40 min (Figure 2b). Thus, Figure 2a gives information on the surface of a Ti-doped Fe_2O_3 semiconductor characterized by an atomic percentage of 10.3%, 10. 7%, 50.4%, and 28.6% for Fe $2p^3$, Ti 2p, O1s, and C1s (sample holder), respectively. After sputtering, the analysis reported in Figure 2b involves the layers below the outermost ones (about 20–30 nm lower). In this case, the atomic percentage of Fe $2p^3$, Ti 2p, O1s, Sn $3d^5$, and C1s are 29.5%, 13.0%, 51.0%, 1.1%, and 5.4%. The ratio between Fe and Ti increases after sputtering due to the procedure of synthesis reported in our previous papers [35], where Ti doping is carried out after a chemical bath deposition of FeOOH/FTO. Furthermore, the FTO conductive layer (SnO_x) began to appear at low atomic percentages.

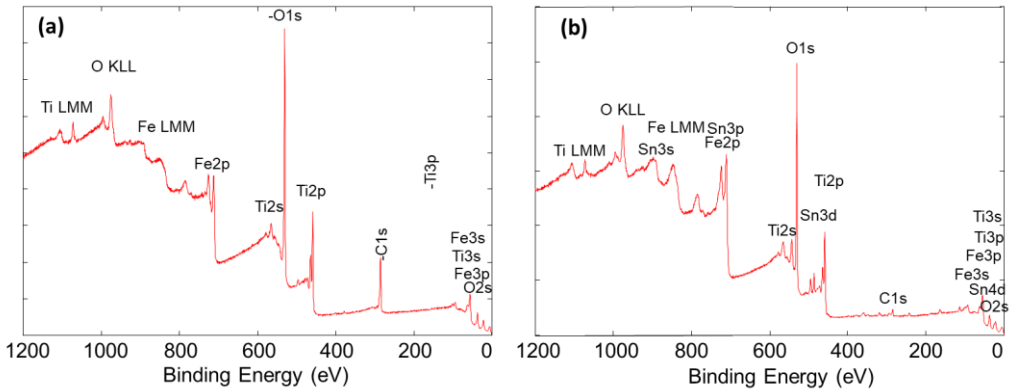

Figure 2. XPS survey spectra of Ti-doped hematite over FTO (**a**) before and (**b**) after argon sputtering.

Figure 3 displays the X-ray diffraction (XRD) patterns of CuO deposited over the hydrophobized GDL and hydrophobic GDL substrate. The procedure of the synthesis, reported in our previous work [36], leads to the formation of monoclinic CuO (JCPDS card number 45-0937) without any presence of metallic Cu or Cu_2O. The crystallite size, calculated by the Debye-Sherrer equation at 35°, is 5.2 nm.

Other morphological characteristics of the photocathode were investigated in a previous study [36] by SEM analysis, confirming the presence of CuO nanoparticles and the homogeneous distribution of a hydrophobic fluoro–ethylene–propylene (FEP) polymer over the GDL, which allows dry hydrogen production from photoelectrochemical water splitting.

2.2. Scalability of PEC Cell and Electrochemical Results

Tandem photoelectrochemical cells were prepared and assembled with a solid anion exchange membrane, working as both an electrolyte and gas separator, between the photoanode (Ti-doped α-Fe_2O_3/FTO), directly exposed to solar irradiation, and the photocathode (CuO/GDL). Figure S1 shows a sketch of the easily scalable tandem PECs: the standard cell having an active area of 0.25 cm^2 as employed in our previous publications [35–37], a 7.5 cm^2 rectangular cell, and a 25 cm^2 square cell.

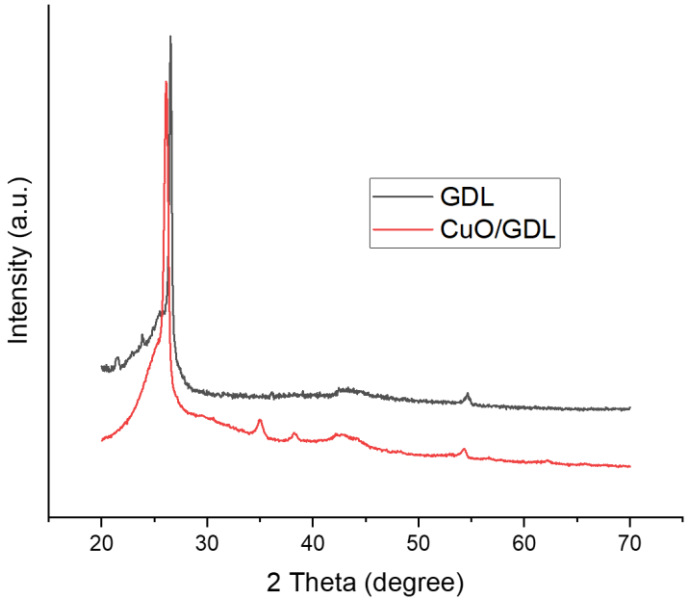

Figure 3. XRD of the CuO/GDL (red line) photocathode and GDL (black line) substrate.

For electrochemical measurements, working and sensing electrodes were connected to a titanium foil in intimate contact with the GDL at the photocathode, while reference and counter electrodes were linked to the conductive FTO glass. A solar simulator directly irradiates the photoanode which adsorbs the UV–Vis wavelengths, while the transmitted or diffused light passes through the transparent membrane and reaches the photocathode. Thus, the appropriate band gaps and band edge bending of the tandem cell semiconductors [35] lead to the evolution of oxygen (photoanode) and hydrogen (photocathode).

Figure 4 shows the results of the on-off experiments (5 s under illumination and 5 s in the dark) in which the photocurrent densities ($J_{light} - J_{dark}$) of the three PECs are directly correlated to the water-splitting reactions. A negative effect of the photocurrent is evident within the scalability; at −0.6 V, i.e., at low bias potential values, the photocurrent decreases from 1.1 mA/cm^2 with the 0.25 cm^2 PEC to 0.42 mA/cm^2 with the 25 cm^2 PEC. These drawbacks, related to the scale-up process, could be explained in terms of optimal clamping between the membrane and photoelectrodes in the 0.25 cm^2 lab cell, resulting in a better and simplified mass transfer of reagents and products and, consequently, in an improved photocurrent density. Furthermore, the electron–hole recombination of the semiconductors increases as a function of larger active areas and distance between the electrons and the FTO conductive layer.

Thus, the main disadvantages of large-area PEC are related to the easier electron–hole recombination, the mass transfer issue from/to the active sites, the difficult path for oxygen escape, and a lower compression force between the photoelectrodes and the electrolyte, mainly in the central part of the large area PEC.

These critical issues can be overcome by improving the interface contact between the photoelectrodes and membrane through an ex-situ assembly procedure using hot or cold pressing with an ionomer glue.

The GEMA concept, "Cell as whole", is illustrated in Figure S2 and employed to improve the interfacial contact between the membrane and photoelectrodes. The GEMA is externally assembled layer by layer, obtaining a solid component that integrates the photoanode, the photocathode, and the membrane. In this process, intimate contact between the membrane and the photoelectrodes can be reached, and the assembly can be visually inspected before the final clamping. The assembly method of these layers requires laser etching/drilling of the FTO transparent glass for a water solution flow towards the interface and oxygen getaway. Moreover, the advantages of the GEMA concept result in an

enhanced oxygen evolution kinetic, straightforward hydration of the anionic membrane, and easy integration in future PEC prototypes.

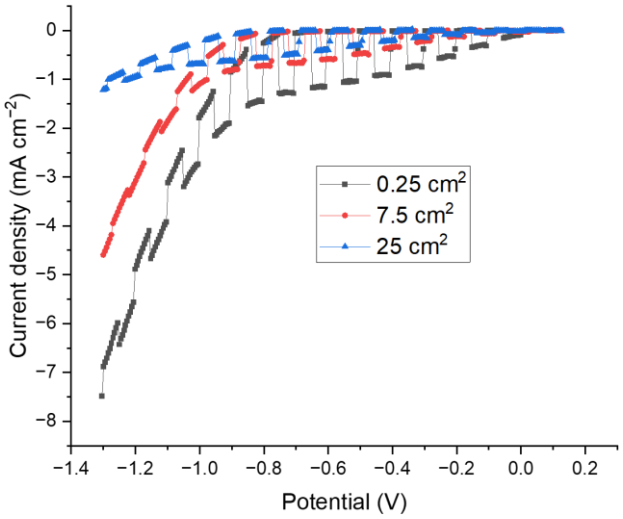

Figure 4. Photocurrent density of the three PEC cells of 0.25 cm^2, 7.5 cm^2, and 25 cm^2 by on-off polarization experiments.

The first attempts to achieve a GEMA were carried out by hot pressing at 60 °C and 20 Kgf cm^{-2}. However, this technique led to facile FTO glass breakage and it was necessary to develop an alternative methodology, which consisted of using an ionomer "glue" (see Section 3.2) to fix the layers together, obtaining a GEMA without glass-breaking issues. The GEMA was tested in the small area test cell, with electrochemical results comparable to those in the conventional configuration. For instance, the polarization curves shown in Figure 5 compare the 4.5 cm^2 conventional clamped PEC (without glue) and 4.5 cm^2 PEC based on the definitive GEMA concept (with glue). The photocurrents in the two PECs were comparable, mainly in our region of interest (below −0.8 V), i.e., at a low bias-assisted region. At −0.6 V bias-assisted potential, the dark current is zero, and there is only a slight difference between the two cells; under illumination, current densities of 0.67 mA cm^{-2} and 0.76 mA cm^{-2} were achieved for the PEC based on the GEMA concept and that assembled without glue, respectively. The current density values at −1.3 V are between 0.25 cm^2 and 7.5 cm^2, as depicted in Figure 4.

A preliminary qualitative examination of Nyquist spectra, obtained from electrochemical impedance spectroscopy (EIS) analysis, enables the differentiation between series or ohmic resistance and polarization resistance. The high-frequency intercept of the semicircles on the x-axis in the Nyquist plots is representative of the ohmic resistance, more precisely referred to as the series resistance (Rs). The polarization resistance (Rp) is then estimated as the difference between the low-frequency intercept in the Nyquist plot and Rs. The combined resistance, represented by the low-frequency intercept on the abscissa in the Nyquist plot (Rs + Rp), corresponds to the differential resistance observed in the polarization curves.

When the system is under illumination, the equivalent electrical circuit comprises an ohmic resistance (series resistance) connected in series with two elements, each formed by a parallel combination of resistance and a constant phase element (CPE). The series resistance reflects the ohmic phenomena, while the R-CPE components are associated with the properties of the electrode-electrolyte interface and the corresponding faradaic processes.

An analysis of the electrochemical impedance spectra shows that the polarization resistance is the rate-determining step.

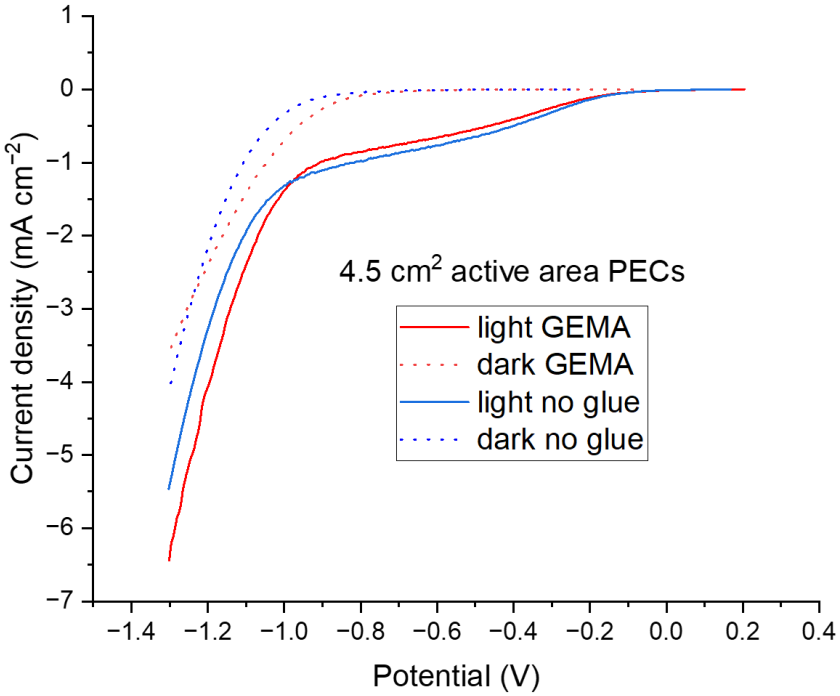

Figure 5. Polarization measurements with a conventional clamped cell and with a GEMA.

Figure 6 shows EIS measurements carried out on a 4.5 cm^2 GEMA in which the Rs (<30 Ω cm^2) and Rp (>250 Ω cm^2 at −0.6 V) were recorded. At −1.3 V, there is no difference between the spectra under illumination and in the dark.

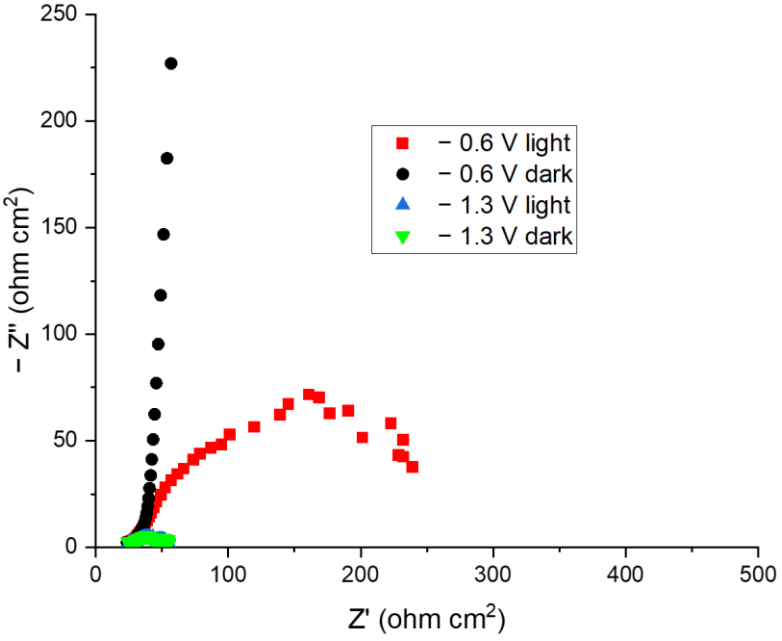

Figure 6. EIS of 4.5 cm^2 GEMA at −0.6 V and −1.3 V under illumination or in the dark.

To scale up the PEC based on non-critical raw semiconductors and increase the efficiency of the solar to hydrogen conversion, many attempts were made to optimize an enhanced interaction between the photoelectrodes and the electrolyte. Figure S3 shows the idea of inserting a glass support below the photocathode to investigate the electrochemical performance in both a 7.5 cm^2 rectangular cell (Figure S4) and a 25 cm^2 square cell (Figure S5). In this case, enthalpy and throughput efficiency achieved a maximum

value of 0.5% at −0.6 V and about 1.0% at about −0.9 V, even if the cell was scaled more than 5 times. Figure S6 displays a similar current density, under illumination and in the dark, obtained with two PEC cells based on drilled or full FTO. As mentioned before, a drilled FTO is necessary for the water inlet and oxygen outlet in the GEMA concept. Finally, the optimized PEC with the use of a glass support at the photocathode, a drilled FTO at the photoanode and ionomeric glue to create a GEMA was investigated for the assessment of enhanced photocurrent. Indeed, Figure S7 reveals a value of the improved photocurrent (0.56 mA/cm^2 at −0.6 V) and, consequently, maximum enthalpy (0.8% at −1 V) and throughput efficiency (3.0% at −1.1 V).

After optimization, square and rectangular PECs with a 40 cm^2 active area were obtained with a procedure detailed in Figure S8. In a 40 cm^2 square clamped PEC, the photocurrent is 0.35 mA cm^{-2} at −0.6 V (Figure 7a). In contrast, the results of rectangular clamped PEC with the same geometric area correspond to a photocurrent of 0.67 mA cm^{-2} at −0.6 V (Figure 7b).

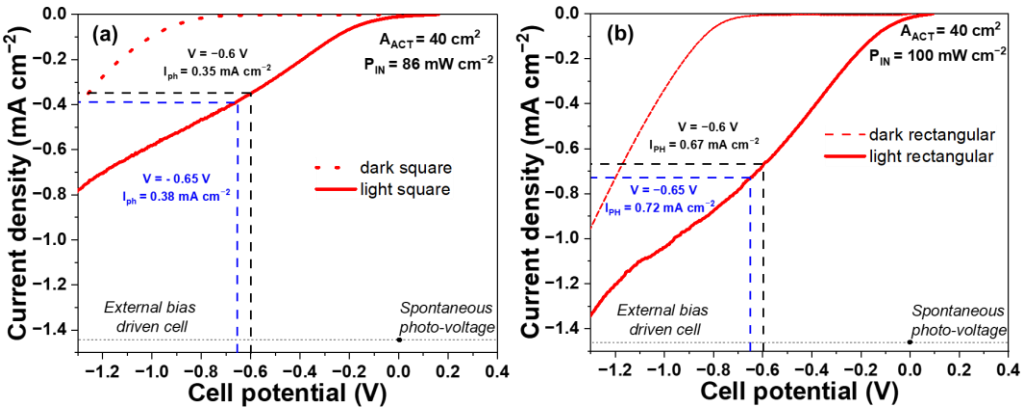

Figure 7. Polarization measurements of (**a**) 40 cm^2 square cell and (**b**) 40 cm^2 rectangular cell.

These results are reflected also in the efficiency values calculated by Equations (1) and (2) in Section 3.6 and displayed in Figure 8. The increase in function of a larger photocurrent (I_{ph}) and a lower bias potential (E_{bias}) normalizes the power irradiation (P_{in}). At a fixed value of E_{bias}, greater photocurrents of the PEC, i.e., the difference between current density under illumination and in the dark, results in higher increases in the efficiency values. Maximum enthalpy efficiencies are 0.37% (Figure 8a) and 0.6% (Figure 8b) at −0.69 V, for the square and rectangular clamped PECs, respectively.

At the same time, throughput efficiency reaches a maximum value of 0.83% (Figure 8c) for the square cell and 1.2% (Figure 8d) for the rectangular clamped PEC.

The rise in dark current density, resulting from the applying a high voltage bias, likely disrupts the photoconversion process. This occurrence may stem from a degradation process at elevated applied potentials, such as the potential reduction of CuO to metallic copper. The applied bias increases the potential differences between the positive electrode (Fe_2O_3) and the negative electrode (CuO). To mitigate this, the voltage bias should be maintained within a practical range where dark current is substantially minimized.

Figure 9 compares the EIS spectra of the 40 cm^2 clamped PECs; Rs and Rp achieve a significant shift toward lower values. The Rs is 200 Ωcm^2 in both PECs, whereas the main issues are related, as usual, to the Rp, which is 1.2 kΩcm^2 in the square cell and less than 800 Ωcm^2 in the rectangular cell at −0.4 V. This value is lower in comparison with the other cell, probably due to a more homogeneous pressure, resulting in improved photo-electrodes-membrane interfaces.

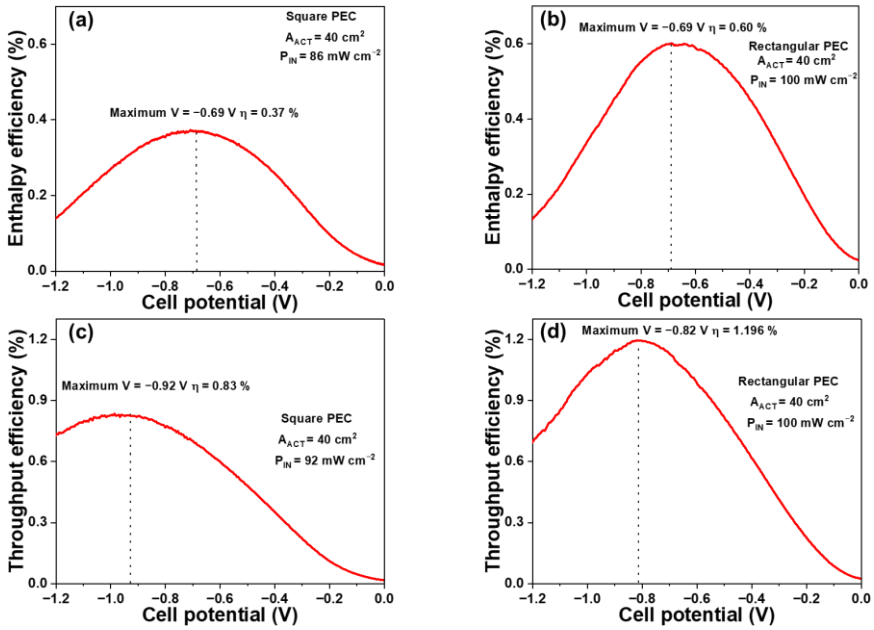

Figure 8. Enthalpy efficiency of 40 cm^2 active area cells: (**a**) square shape and (**b**) rectangular shape; throughput efficiency of 40 cm^2 active area cells: (**c**) square shape and (**d**) rectangular shape.

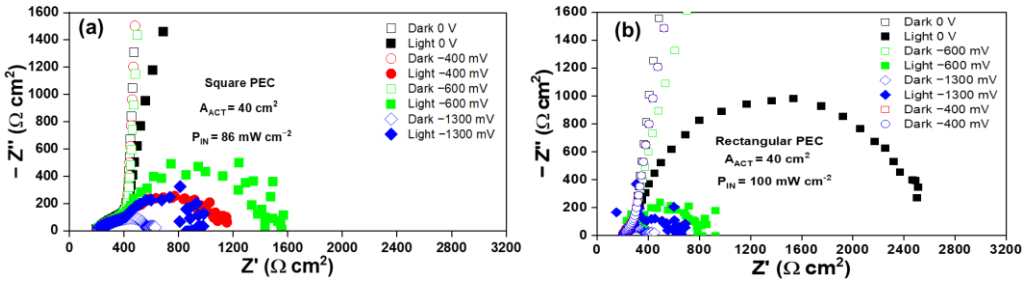

Figure 9. Impedance spectra of (**a**) square cell of 40 cm^2 active area and (**b**) rectangular cell of 40 cm^2 active area.

Short-term durability tests were carried out under a constant current of 15 mA to evaluate the feasibility of this low-cost PEC. The ability to produce hydrogen was demonstrated in our previous works [35–37] by connecting a tube from the photocathode outlet to a gas chromatograph. As shown in Figure 10, the potential is almost stable for about 5 h achieving a value of about −0.6 V under illumination and ranging from −1.0 to −1.1 V under dark conditions. Furthermore, under irradiation, the current increases when a KOH-refilling of the cell is adopted, such as at 1 h or 2.8 h.

Currently, an applied bias is commonly used to overcome the kinetic and thermodynamic barriers of photoelectrochemical cells, such as minimising the electron–hole recombination of photoelectrodes and accelerating the charge transfer from the photoanode to the photocathode, for photoelectrochemical WS at a relatively suitable solar to hydrogen efficiency (>10% for commercial and economic purposes) [38]. For instance, Qiu et al. [39] reported a study with Mo-$BiVO_4$ on an engineered cone-shaped nanophotonic structure and after the deposition of Fe(Ni)OOH, the photocurrent density was 5.8 mAcm^{-2} at 1.23 V of applied bias. Among the various co-catalysts, cobalt phosphate (CoPi) complexes were widely used to enhance the photoelectrochemical efficiency with outstanding catalytic activity demonstrated for both anodic and cathodic processes [40]. However, this work investigated tandem cells, based on non-critical raw materials for the European Union (EU), and since Bismuth (BiVO) and cobalt (cobalt phosphate) are unfortunately included in the EU critical raw materials (CRM) list, they were not considered for this work.

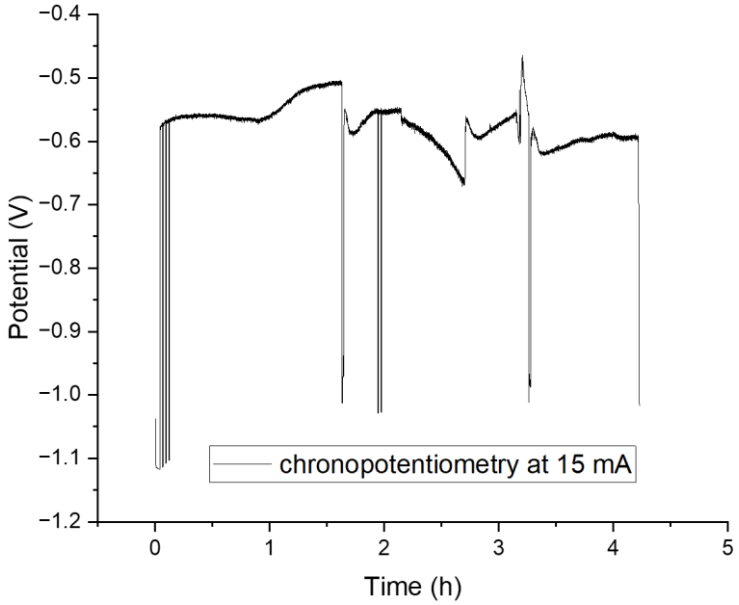

Figure 10. Chronopotentiometry at 15 mA with the 40 cm^2 rectangular PEC.

The biggest challenge of this technology for large-scale commercialization is achieving a bias-free WS PEC employing inexpensive and earth-abundant materials in combination with the facile scalability of the components. From our point of view, this is achievable in the future by enhancing the light intensity adsorption of the tandem cell through optimization of both the electrode thickness and the use of efficient non-CRM co-catalysts such as nickel alloys, as well as the substitution of the polymeric membrane with a better performing solid electrolyte.

3. Materials and Methods

3.1. Synthesis of Photoelectrodes

Hematite-based photoanodes were prepared on scalable clamped PEC following the procedure reported for 0.25 cm^2 lab cells [35]. Briefly, a large glass reactor, containing 0.15 $mol \cdot L^{-1}$ $FeCl_3 \cdot 6H_2O$ (Sigma-Aldrich, St. Louis, MO, USA, 99%) and 1 M $NaNO_3$ (Sigma-Aldrich, St. Louis, MO, USA, 99%) precursors, was used for the chemical bath made at 100 °C for 6 h to obtain FeOOH/drilled FTO. Successively, a dip-coating of the FeOOH/FTO electrode was implemented by a 1 min immersion in a 0.1 $mol \cdot L^{-1}$ Ti-isopropoxide solution in isopropanol. Finally, the anode was subjected to a heat treatment at 650 °C for 1 h to obtain the α-Fe_2O_3/FTO phase.

The preparation of CuO/hydrophobized GDL (Sigracet 39BB) was reported in our previous work [36]. Herein, metallic Cu derived from the reduction of CuO obtained by the oxalate method was deposited over a previously hydrophobized GDL (+7% FEP) by spraying with an airbrush (HP-CPlus from IWATA High Performance HP-C Plus, Portland, OR, USA). After that, a chemical oxidation of Cu/GDL was performed in a 2.5 $mol \cdot L^{-1}$ aqueous solution of sodium hydroxide (NaOH, Scharlab, Barcelona, Spain, extra pure) and 0.125 $mol \cdot L^{-1}$ ammonium persulfate ($(NH_4)_2S_2O_8$, Sigma-Aldrich, St. Louis, MO, USA, 98%) for 11 min followed by a thermal treatment in air at 300 °C for 1 h. The deposition of CuO over the GDL of 100 cm^2 geometrical area was 2 mg cm^{-2}. Finally, the area was cut to achieve rectangular or square 40 cm^2 photocathodes.

3.2. Anion Membrane and Ionomer Glue Preparation

A commercial FAA3-50 anion exchange membrane (FumaTech, Bietigheim-Bissingen, Germany) was received in bromide form. It was firstly exchanged with 1 M NaCl to purify it from the residues of production chemicals and subsequently, it was subjected to

an anion-exchange process in a 1 M KOH aqueous solution for 24 h, before assembly to exchange the chloride by hydroxide.

Commercial FAA3 shredded film (FumaTech) was used to prepare the ionomer dispersion. The ionomer was supplied in bromide form. It was exchanged in 1 M KOH for 24 h at room temperature, then washed until the filtered water reached a neutral pH, and finally, it was dried at 40 °C in an oven for 2 h. The ionomer in the OH^- form was solubilized in an alcoholic solution of n-propanol and ethanol (1:1 wt) at room temperature under stirring to have ~5 wt% dispersion and used as a glue over the photoanode and photocathode before the assembly.

3.3. Assembly of the Tandem Photoelectrochemical Cell

Clamped photoelectrochemical cells were assembled with a scalable method of up to 40 cm^2 rectangular or square PEC.

The FAA3 ionomer glue in hydroxide form was deposited on both the photoanode (PA) and photocathode (PC) surfaces by adding 25 μL cm^{-2} ionomer loading (FAA3-OH, 5 wt% in 1:1 ethanol-n-propanol mixture) by drop casting. The FAA3-50, appropriately hydrated by a solution of 1 M KOH for 24 h, was assembled and clamped between the PA and PC to ensure good contact in the three space regions (photoelectrodes/electrolyte) of the GEMA.

The PEC cells were tested in a solar simulator (Oriel Newport, Irvine, CA, USA) in a horizontal position by maintaining 100, 92, or 86 mW cm^{-2} of power irradiation, as revealed by a calibrated photovoltaic cell before each experiment.

3.4. Physicochemical Characterization

An X'Pert 3710 X-Ray (Philips, Eindhoven, The Netherlands) diffractometer with a Cu-Kα source at 40 kV and 20 mA was employed for X-ray diffraction (XRD) analysis. In contrast, the Debye–Scherrer equation was used for the calculation of the crystallite size.

A Physical Electronics (PHI) 5800-01 X-ray photoelectron spectrometer, Chanhassen, MN, USA, employing Alk_α as a monochromatic X-ray source at a power of 350 W was used to analyse the surface chemistry of the synthesized electrocatalysts.

3.5. Electrochemical Tests

The working and sensing electrodes (WE, SE) were connected to the FTO on the photoanode. The connection of the reference and counter electrodes (RE, CE) was ensured by a Ti sheet in intimate contact with the GDL on the photocathode.

Linear sweep voltammetry tests were performed between the open circuit potential (OCP) value and a bias of −1.3 V, recording the curves in the dark and under illumination conditions.

Impedance spectra were carried out at short circuit, with a bias of −0.4 V, −0.6 V, and −1.3 V under illumination and in the dark. The recorded frequencies were within a range of 1 KHz−0.1 Hz (10 mV_{rms}) and the results were obtained by a frequency response analyser (FRA) supported on Metrohm Autolab potentiostat/galvanostat, Ultrecht, The Netherlands.

Chronopotentiometry was carried out at 15 mA to investigate the potential over time for 5 h.

3.6. Efficiency of the PEC

The efficiencies of photoelectrochemical cells were calculated as reported in Equations (1) and (2) and previous papers [35–37].

$$\text{Enthalpy efficiency: } \eta = Iph(\Delta H/nF - Ebias)/Pin = Iph(Etn - Ebias)/Pin \quad (1)$$

$$\text{Throughput efficiency: } \eta = Iph(\Delta H/nF)/(Pin + Iph\ Ebias) = Iph\ Etn/(Pin + Iph\ Ebias) \quad (2)$$

where Etn = 1.48 V, Erev = 1.23 V, Ebias ≡ V, Pin ≡ mW cm^{-2}, and Iph = I light − I dark ≡ mA cm^{-2}.

For instance, to calculate the enthalpy efficiency from electrochemical measurements, the photocurrent (Iph), achieved at one bias-potential (Ebias), was multiplied for the difference between the thermoneutral potential (Etn) and the bias potential and divided for the power irradiation (Pin) calculated with a calibrated photovoltaic reference cell for each experiment.

4. Conclusions

Tandem photoelectrochemical cells (PECs) were equipped with non-critical raw materials, such as a Ti-doped hematite photoanode and a CuO/hydrophobized GDL photocathode. The scalability of such devices was investigated in rectangular or square cells between 0.25 cm^2 and 40 cm^2. The concept of a glass electrode membrane assembly (GEMA) was investigated for the first time with an ionomeric glue to enhance the interfacial photoelectrodes/electrolyte interfaces. After optimization, the scaled rectangular 40 cm^2 PEC showed a maximum enthalpy efficiency and throughput efficiency at a low-bias voltage of 0.6% and 1.2%, larger than the 40 cm^2 square-clamped cell (0.4% and 0.8%). This research could be the starting point for obtaining prototypes to produce pure hydrogen by renewable sunlight.

Supplementary Materials: The following supporting information can be downloaded at: https://www.mdpi.com/article/10.3390/catal14020098/s1, Figure S1: Photographs of the three developed PECs: 0.25 cm^2, 7.5 cm^2 and 25 cm^2; Figure S2: GEMA and its mechanism with drilled FTO; Figure S3: Sketch of the concept to increase the efficiency of tandem PEC; Figure S4: (a) Current density under illumination and in the dark, (b) enthalpy and (c) throughput efficiency of the 7.5 cm^2 rectangular cell; Figure S5: (a) Current density under illumination and in the dark, (b) enthalpy and (c) throughput efficiency of the 25 cm^2 square cell; Figure S6: Current density under illumination and in the dark for the tandem PEC based on (a) full FTO and (b) drilled FTO; Figure S7: (a) Current density under illumination and in the dark, (b) enthalpy and (c) throughput efficiency of an optimized 6 cm^2 square cell with ionomeric glue; Figure S8: Preparation of hematite/FTO starting with FeOOH/drilled FTO.

Author Contributions: Conceptualization, V.B., A.S.A. and G.G.; methodology, A.S.A. and V.B.; synthesis, C.L.V. and A.C.; investigation, C.L.V., S.T., A.C., G.G., O.B. and G.M.; data curation, C.L.V. and S.T.; writing—original draft preparation, C.L.V.; writing—review and editing, S.T., V.B., A.C., G.G. and O.B. All authors have read and agreed to the published version of the manuscript.

Funding: Authors gratefully acknowledge funding from the European Union's Horizon 2020 research and innovation programme under grant agreement no. 760930 (FotoH2 project).

Data Availability Statement: Data are available upon request to the corresponding authors.

Conflicts of Interest: The authors declare no conflicts of interest.

References

1. Barbir, F. Transition to Renewable Energy Systems with Hydrogen as an Energy Carrier. *Energy* **2009**, *34*, 308–312. [CrossRef]
2. Tian, J.; Yu, L.; Xue, R.; Zhuang, S.; Shan, Y. Global Low-Carbon Energy Transition in the Post-COVID-19 Era. *Appl. Energy* **2022**, *307*, 118205. [CrossRef] [PubMed]
3. Dhar, A.; Naeth, M.A.; Jennings, P.D.; Gamal El-Din, M. Perspectives on Environmental Impacts and a Land Reclamation Strategy for Solar and Wind Energy Systems. *Sci. Total Environ.* **2020**, *718*, 134602. [CrossRef] [PubMed]
4. Rabaia, M.K.H.; Abdelkareem, M.A.; Sayed, E.T.; Elsaid, K.; Chae, K.J.; Wilberforce, T.; Olabi, A.G. Environmental Impacts of Solar Energy Systems: A Review. *Sci. Total Environ.* **2021**, *754*, 141989. [CrossRef]
5. Sadorsky, P. Wind Energy for Sustainable Development: Driving Factors and Future Outlook. *J. Clean. Prod.* **2021**, *289*, 125779. [CrossRef]
6. Pan, Y.; Zhang, H.; Zhang, B.; Gong, F.; Feng, J.; Huang, H.; Vanka, S.; Fan, R.; Cao, Q.; Shen, M.; et al. Renewable Formate from Sunlight, Biomass and Carbon Dioxide in a Photoelectrochemical Cell. *Nat. Commun.* **2023**, *14*, 1013. [CrossRef] [PubMed]
7. Vorlet, S.L.; De Cesare, G. A Comprehensive Review on Geomembrane Systems Application in Hydropower. *Renew. Sustain. Energy Rev.* **2024**, *189*, 113951. [CrossRef]
8. Alhuyi-Nazari, M.; Mukhtar, A.; Yasir, A.S.H.M.; Ahmadi, M.H.; Kumar, R.; Luong, T. Applications of Geothermal Sources for Absorption Chillers as Efficient and Clean Cooling Technologies for Buildings: A Comprehensive Review. *J. Build. Eng.* **2024**, *82*, 108340. [CrossRef]

9. Sadekin, S.; Zaman, S.; Mahfuz, M.; Sarkar, R. Nuclear Power as Foundation of a Clean Energy Future: A Review. *Energy Procedia* **2019**, *160*, 513–518. [CrossRef]
10. Vilanova, A.; Lopes, T.; Mendes, A. Large-Area Photoelectrochemical Water Splitting Using a Multi-Photoelectrode Approach. *J. Power Sources* **2018**, *398*, 224–232. [CrossRef]
11. Landman, A.; Halabi, R.; Dias, P.; Dotan, H.; Mehlmann, A.; Shter, G.E.; Halabi, M.; Naseraldeen, O.; Mendes, A.; Grader, G.S.; et al. Decoupled Photoelectrochemical Water Splitting System for Centralized Hydrogen Production. *Joule* **2020**, *4*, 448–471. [CrossRef]
12. Kelly, N.A.; Gibson, T.L. Solar Energy Concentrating Reactors for Hydrogen Production by Photoelectrochemical Water Splitting. *Int. J. Hydrogen Energy* **2008**, *33*, 6420–6431. [CrossRef]
13. Aralekallu, S.; Sannegowda Lokesh, K.; Singh, V. Advanced Bifunctional Catalysts for Energy Production by Electrolysis of Earth-Abundant Water. *Fuel* **2024**, *357*, 129753. [CrossRef]
14. Niblett, D.; Delpisheh, M.; Ramakrishnan, S.; Mamlouk, M. Review of next Generation Hydrogen Production from Offshore Wind Using Water Electrolysis. *J. Power Sources* **2024**, *592*, 233904. [CrossRef]
15. Sharshir, S.W.; Joseph, A.; Elsayad, M.M.; Tareemi, A.A.; Kandeal, A.W.; Elkadeem, M.R. A Review of Recent Advances in Alkaline Electrolyzer for Green Hydrogen Production: Performance Improvement and Applications. *Int. J. Hydrogen Energy* **2024**, *49*, 458–488. [CrossRef]
16. Daoudi, C.; Bounahmidi, T. Overview of Alkaline Water Electrolysis Modeling. *Int. J. Hydrogen Energy* **2024**, *49*, 646–667. [CrossRef]
17. Shiva Kumar, S.; Himabindu, V. Hydrogen Production by PEM Water Electrolysis—A Review. *Mater. Sci. Energy Technol.* **2019**, *2*, 442–454. [CrossRef]
18. Chatterjee, P.; Ambati, M.S.K.; Chakraborty, A.K.; Chakrabortty, S.; Biring, S.; Ramakrishna, S.; Wong, T.K.S.; Kumar, A.; Lawaniya, R.; Dalapati, G.K. Photovoltaic/Photo-Electrocatalysis Integration for Green Hydrogen: A Review. *Energy Convers. Manag.* **2022**, *261*, 115648–115685. [CrossRef]
19. Hogerwaard, J.; Dincer, I.; Naterer, G.F. Experimental Investigation and Optimization of Integrated Photovoltaic and Photoelectrochemical Hydrogen Generation. *Energy Convers. Manag.* **2020**, *207*, 112541. [CrossRef]
20. Carrette, L.; Friedrich, K.A.; Stimming, U. Fuel Cells: Principles, Types, Fuels, and Applications. *ChemPhysChem* **2000**, *1*, 162–193. [CrossRef]
21. Peighambardoust, S.J.; Rowshanzamir, S.; Amjadi, M. Review of the Proton Exchange Membranes for Fuel Cell Applications. *Int. J. Hydrogen Energy* **2010**, *35*, 9349–9384. [CrossRef]
22. Lamy, C. From Hydrogen Production by Water Electrolysis to Its Utilization in a PEM Fuel Cell or in a SO Fuel Cell: Some Considerations on the Energy Efficiencies. *Int. J. Hydrogen Energy* **2016**, *41*, 15415–15425. [CrossRef]
23. Mclean, G.F.; Niet, T.; Prince-Richard, S.; Djilali, N. An Assessment of Alkaline Fuel Cell Technology. *Int. J. Hydrogen Energy* **2002**, *27*, 507–526. [CrossRef]
24. Serov, A.; Artyushkova, K.; Niangar, E.; Wang, C.; Dale, N.; Jaouen, F.; Sougrati, M.T.; Jia, Q.; Mukerjee, S.; Atanassov, P. Nano-Structured Non-Platinum Catalysts for Automotive Fuel Cell Application. *Nano Energy* **2015**, *16*, 293–300. [CrossRef]
25. Trimm, D.L. Coke Formation and Minimisation during Steam Reforming Reactions. *Catalysis Today* **1997**, *37*, 233–238. [CrossRef]
26. Lopes, T.; Dias, P.; Andrade, L.; Mendes, A. An Innovative Photoelectrochemical Lab Device for Solar Water Splitting. *Sol. Energy Mater. Sol. Cells* **2014**, *128*, 399–410. [CrossRef]
27. Ciesielski, P.N.; Hijazi, F.M.; Scott, A.M.; Faulkner, C.J.; Beard, L.; Emmett, K.; Rosenthal, S.J.; Cliffel, D.; Kane Jennings, G. Photosystem I—Based Biohybrid Photoelectrochemical Cells. *Bioresour. Technol.* **2010**, *101*, 3047–3053. [CrossRef] [PubMed]
28. Vilanova, A.; Lopes, T.; Spenke, C.; Wullenkord, M.; Mendes, A. Optimized Photoelectrochemical Tandem Cell for Solar Water Splitting. *Energy Storage Mater.* **2018**, *13*, 175–188. [CrossRef]
29. Ahmed, M.; Dincer, I. A Review on Photoelectrochemical Hydrogen Production Systems: Challenges and Future Directions. *Int. J. Hydrogen Energy* **2019**, *44*, 2474–2507. [CrossRef]
30. Juodkazyte, J.; Šebeka, B.; Savickaja, I.; Jagminas, A.; Jasulaitiene, V.; Selskis, A.; Kovger, J.; Mack, P. Study on Copper Oxide Stability in Photoelectrochemical Cell Composed of Nanostructured TiO_2 and Cu_xO Electrodes. *Electrochim. Acta* **2014**, *137*, 363–371. [CrossRef]
31. Rojas, V.; Navarrete, E.; Román, J.; Ballesteros, L.; Cáceres, G.; Díaz, R.; Schrebler, R.; Córdova, R.; Grez, P.; Henríquez, R.; et al. Study about an Assembly of Iron(III) Hexacyanoferrate(II) and α-Fe_2O_3 as a Secondary Photocell: Part 1. Synthesis, Characterization and Photoelectrochemical Properties of FTO/α-Fe_2O_3/$KFe[Fe(CN)_6]_3$ Electrode System. *J. Electroanal. Chem.* **2020**, *860*, 113913. [CrossRef]
32. Jiang, C.; Moniz, S.J.A.; Wang, A.; Zhang, T.; Tang, J. Photoelectrochemical Devices for Solar Water Splitting-Materials and Challenges. *Chem. Soc. Rev.* **2017**, *46*, 4645–4660. [CrossRef] [PubMed]
33. Giacoppo, G.; Trocino, S.; Lo Vecchio, C.; Baglio, V.; Díez-García, M.I.; Aricò, A.S.; Barbera, O. Numerical 3D Model of a Novel Photoelectrolysis Tandem Cell with Solid Electrolyte for Green Hydrogen Production. *Energies* **2023**, *16*, 1953. [CrossRef]
34. Aricò, A.S.; Girolamo, M.; Siracusano, S.; Sebastian, D.; Baglio, V.; Schuster, M. Polymer Electrolyte Membranes for Water Photo-Electrolysis. *Membranes* **2017**, *7*, 25. [CrossRef] [PubMed]

35. Lo Vecchio, C.; Trocino, S.; Zignani, S.C.; Baglio, V.; Carbone, A.; Díez-García, M.I.; Contreras, M.; Gómez, R.; Aricò, A.S. Enhanced Photoelectrochemical Water Splitting at Hematite Photoanodes by Effect of a Nife-Oxide Co-Catalyst. *Catalysts* **2020**, *10*, 525. [CrossRef]
36. Trocino, S.; Lo Vecchio, C.; Zignani, S.C.; Carbone, A.; Saccà, A.; Baglio, V.; Gómez, R.; Aricò, A.S. Dry Hydrogen Production in a Tandem Critical Raw Material-Free Water Photoelectrolysis Cell Using a Hydrophobic Gas-Diffusion Backing Layer. *Catalysts* **2020**, *10*, 1319. [CrossRef]
37. Lo Vecchio, C.; Trocino, S.; Giacoppo, G.; Barbera, O.; Baglio, V.; Díez-García, M.I.; Contreras, M.; Gómez, R.; Aricò, A.S. Water Splitting with Enhanced Efficiency Using a Nickel-Based Co-Catalyst at a Cupric Oxide Photocathode. *Catalysts* **2021**, *11*, 1363. [CrossRef]
38. Zhang, H.; Wang, H.; Xuan, J. Rational Design of Photoelectrochemical Cells towards Bias-Free Water Splitting: Thermodynamic and Kinetic Insights. *J. Power Sources* **2020**, *462*, 228113. [CrossRef]
39. Qiu, Y.; Liu, W.; Chen, W.; Zhou, G.; Hsu, P.C.; Zhang, R.; Liang, Z.; Fan, S.; Zhang, Y.; Cui, Y. Efficient Solar-Driven Water Splitting by Nanocone $BiVO_4$-Perovskite Tandem Cells. *Sci. Adv.* **2016**, *2*, e1501764. [CrossRef]
40. Kment; Sivula, K.; Naldoni, A.; Sarmah, S.P.; Kmentová, H.; Kulkarni, M.; Rambabu, Y.; Schmuki, P.; Zbořil, R. FeO-Based Nanostructures and Nanohybrids for Photoelectrochemical Water Splitting. *Prog. Mater. Sci.* **2020**, *110*, 100632. [CrossRef]